A 200 μm-PERIOD LASER-DRIVEN UNDULATOR*

F. Toufexis, T. Tang, S.G. Tantawi, SLAC, Menlo Park, CA 94025, USA
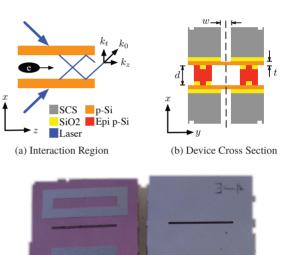
Abstract

To reduce the linac energy required for a given synchrotron radiation wavelength, and hence the size of the device, a smaller undulator period with sufficient field strength is needed. In this work, a microfabricated, laser-driven undulator with 200 μm undulator period is proposed. A transverse electric (TE) wave that co-propagates with the electron beam is excited between two polysilicon thin films, having a gap of 16.5 μm. The mode that is excited is a deflecting mode and causes the electron beam to wiggle. The device is fabricated on a silicon wafer, using conventional silicon micromachining techniques. A single polysilicon thin film is supported on a silicon chip, which has a slit from the back to allow delivery of the laser beam. Two such chips are bonded together to form a 16.5 μm gap, within which the electron beam passes through. The final device has dimensions 1cm x 1cm x 1.1mm and has approximately 35 undulator periods. In this paper, the model, design, fabrication, and cold measurements of the device are reported.

INTRODUCTION

Traditionally, coherent emission of short wavelength electromagnetic radiation employed undulators – devices that generate a periodic magnetic field – made of permanent magnets. Such undulators present several limitations on how short their period can be, while maintaining reasonable field strength and beam aperture. These limitations, along with the resonance condition between the electrons' oscillatory motion, including relativistic and Doppler effects, and the wavelength of the emitted light, require very high-energy beams, making a tabletop free electron laser (FEL) prohibitive. In order to shrink an FEL, a smaller linac and therefore lower beam energy is required. A smaller undulator period is therefore required, while maintaining sufficient field strength. However, the undulator wavelength cannot be too small – for example using directly a laser beam – because the emittance requirements make it infeasible to operate as a laser [1]. Alternatives to traditional undulators are superconducting magnet-based undulators [2], photonic crystal undulators [3], and microwave undulators [4]. Recently laser driven undulators have been developed [5–8].

In this work, a novel laser–driven undulator is proposed. Figure 1a outlines the principle of operation of the proposed device. A parallel plate dielectric waveguide is used as the interaction region. A TE wave is excited with a 10.6 μm silicon dioxide (CO2) laser. The angle of incidence is chosen so that a specific undulator wavelength is produced. The electron bunch co–propagates with the TE wave, producing an effective undulator wavelength that is larger than the

excitation wavelength. The waveguide is formed by two thin polycrystalline silicon (p-Si) films, supported on two single crystal silicon (SCS) dies that are bonded together, as shown in Figure 1b. A thicker epitaxially grown polycrystalline silicon (epi p-Si) layer, along with sacrificial silicon oxide (SiO2) layers are used to define the gap between the two plates of the waveguide, as well as assist in etching the backside trench, without affecting the plates of the waveguide. Figure 1c shows the two sides of a single die before assembly. Note that in Figure 1c, the SiO2 has not been etched, and the thin film covering the trench has been removed, for better visibility. The devices were fabricated in the Stanford Nanofabrication Facility (SNF) [9].

(a) Interaction Region　　　　(b) Device Cross Section

(c) Fabricated Die before Assembly

Figure 1: Proposed Device Overview.

ANALYTICAL MODEL & DESIGN

Eigen Modes in Infinite Metallic Parallel Plate Waveguide

In this section, solutions to the Time Harmonic Maxwell's equations are sought for the case of the infinite parallel metallic plate waveguide. Analysis starts with this structure, since it is a very good approximation of the fields inside the interaction region of the undulator. The structure has a finite height d in the x–direction, is infinite in y and z–directions, and waves travel along the z direction. Fields are assumed to vary with time as $e^{-j\omega t}$, and therefore, a field propagating in the positive z direction has a z–dependence of the form $e^{jk_z z}$, where $\omega = \frac{2\pi c}{\lambda_0}$ is the field angular frequency, $k_0 = \frac{2\pi}{\lambda_0}$ is the free space propagation constant, $k_z = \frac{2\pi}{\lambda_G}$ is the propagation

constant in z–direction, $k_t = \frac{\pi}{d} = \sqrt{k_0^2 - k_z^2}$ is the transverse propagation constant, λ_0 is the free space wavelength, and λ_G is the wavelength inside the waveguide.

Following the methodology in [10], the eigen modes of this waveguide can be split into TE and transverse magnetic (TM) fields. Analysis begins by separating the transverse and longitudinal to z fields, and replacing $\frac{\partial}{\partial z} = jk_z$. TE solutions are found by finding an expression for H_z that satisfies the wave equation, and replacing it in Maxwell's equations along with $E_z = 0$:

$$H_z = jE_0 \frac{k_t}{\omega\mu} \sin(k_t x)\, e^{-j(\omega t - k_z z)} \quad (1)$$

$$\mathbf{H}_t^{TE} = j\frac{k_z}{k_t^2}\nabla_t H_z = -\hat{\mathbf{x}}E_0 \frac{k_z}{\omega\mu}\cos(k_t x)\, e^{-j(\omega t - k_z z)} \quad (2)$$

$$\mathbf{E}_t^{TE} = -j\frac{\omega\mu}{k_t^2}(\hat{\mathbf{z}}\times\nabla_t H_z) = \hat{\mathbf{y}}E_0\cos(k_t x)\, e^{-j(\omega t - k_z z)} \quad (3)$$

TM solutions are found by finding an expression for E_z that satisfies the wave equation, and replacing it in Maxwell's equations along with $H_z = 0$:

$$E_z = jE_0 \frac{k_t}{k_z}\cos(k_t x)\, e^{-j(\omega t - k_z z)} \quad (4)$$

$$\mathbf{E}_t^{TM} = j\frac{k_z}{k_t^2}\nabla_t E_z = \hat{\mathbf{x}}E_0\sin(k_t x)\, e^{-j(\omega t - k_z z)} \quad (5)$$

$$\mathbf{H}_t^{TM} = j\frac{\omega\epsilon}{k_t^2}(\hat{\mathbf{z}}\times\nabla_t E_z) = \hat{\mathbf{y}}E_0\frac{\omega\epsilon}{k_z}\sin(k_t x)\, e^{-j(\omega t - k_z z)} \quad (6)$$

Comparing Equations (3) and (5), in TE modes, the electric field on the walls of the waveguide is zero, while in TM modes the electric field is maximum. Therefore the TE modes are the most suitable for an undulator since the peak electric fields is in the center of the waveguide.

Undulating Mechanism

The basic theory of a microwave undulator cavity was presented in [11]. When electrons interact with a forward and backward wave, the equivalent undulator wavelength is given by:

$$\lambda_u = \frac{\lambda_0}{1 \pm \frac{\lambda_0}{\lambda_G}} \quad (7)$$

where the plus sign corresponds to the electromagnetic (EM) wave counter–propagating with the electrons, and the minus sign corresponds to the EM wave co–propagating with the electrons. These two cases are referred to as short–period and long–period undulation respectively. Therefore in order to have an undulator wavelength longer than the EM wave wavelength, the wave must co–propagate with he electrons.

For a relativistic electron, the equation of motion is given by:

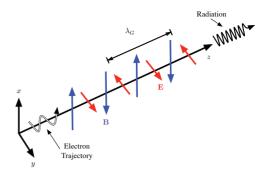$$\mathbf{F} = -q_e\left[\mathbf{E} + \beta c\,(\hat{\mathbf{z}}\times\mathbf{B})\right] \quad (8)$$

Figure 2: Electron Trajectory in TE Wave, adapted from [11].

Replacing (1), (2), and (3) into (8) yields:

$$\mathbf{F} = -\hat{\mathbf{y}}q_e E_0\left(1 - \beta\frac{\lambda_0}{\lambda_G}\right)\cos(k_t x)\cos\left(2\pi\frac{z}{\lambda_u}\right) \quad (9)$$

The wiggling is a result of both the electric and magnetic field, which although mostly cancel each other, given a large E_0, the interaction is still significant. Comparing Equation (9) with the traditional permanent magnet undulator [11], yields an equivalent magnetic field:

$$B_{eq} = \frac{E_0}{\beta c}\left(1 - \beta\frac{\lambda_0}{\lambda_G}\right) \approx \frac{E_0}{c}\left(1 - \frac{\lambda_0}{\lambda_G}\right) \quad (10)$$

Equation (9) therefore describes the motion inside an undulator with:

$$\lambda_u = \frac{\lambda_0}{1 - \frac{\lambda_0}{\lambda_G}} \qquad K = \frac{q_e E_0 \lambda_u}{2\pi c^2 m_0}\left(1 - \frac{\lambda_0}{\lambda_G}\right) \quad (11)$$

Figure 2 shows an overview of the electron trajectory and field configuration of the proposed device.

TE Modes in Parallel Plate Dielectric Waveguide

Figure 3a presents the optical model of the proposed undulator. A laser beam hits the top of the waveguide at an angle θ_0. Part of it gets transmitted in region *II* and the rest gets reflected in region *I*. The transmitted beam travels in region *II* with a different propagation constant and angle, because of the change in refractive index, and gets partially reflected and partially transmitted at the boundary between regions *II* and *III*. Depending on the choice of dimensions, the structure in Figure 3a can behave as a waveguide in z–direction, operating at a weakly confined TE eigen mode.

For a given undulator wavelength, the corresponding waveguide wavelength from Equation (11) is obtained, that determines $k_z = \frac{2\pi}{\lambda_G}$. Also given the excitation free space wavelength λ_0, the propagation constant $k_0 = \frac{2\pi}{\lambda_0}$ is determined. Therefore, to achieve a given undulator wavelength, the angle the laser beams forms with the surface is $\theta_0 = \arccos\left(\frac{k_z}{k_0}\right)$. In order for the structure of Figure 3a to behave as a waveguide in z–direction, the waves in all three areas have to travel with the same propagation constant k_z. For a given medium with refractive index n_i, the

FEL Technology and Hardware: Undulators, Magnets, Photon Diagnostics and Beamlines

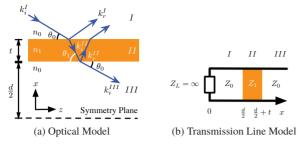(a) Optical Model   (b) Transmission Line Model

Figure 3: Parallel Plate Dielectric Waveguide Model.

transverse to z propagation constant k_t^i can then be determined from $k_t^i = \sqrt{k_i^2 - k_z^2}$, where $k_i = n_i\, k_0$ represents the propagation constant in that medium. In that medium $\theta_i = \arccos\left(\frac{k_z}{k_i}\right) = \arccos\left(\frac{k_z}{n_i k_0}\right)$.

The problem can be analysed separately in x and z coordinates. In the z–direction a TE wave – of some distribution in x – travels with a propagation constant k_z. In the x–direction, standing waves are formed in each region, that satisfy the boundaries between regions. In each region, the standing wave is formed by a forward and backward in the x–direction wave, that travels in region i with a propagation constant k_t^i. The symmetry plane $x = 0$ is a perfect magnetic wall for the eigen mode of interest, since it has maximum tangential electric field and zero tangential magnetic field. The waveguide can therefore be analysed in the x–direction as a transmission line problem, where the voltage represents the electric field E_y and the current represents the magnetic field H_z. Each region with a refractive index n_i has a wave impedance Z_i, and the system is terminated at $x = 0$ with a $Z_L = \infty$. The transmission line equivalent model of the undulator is shown in Figure 3b. Using transmission line theory, the transverse to x fields in each region can be written as:

$$\begin{bmatrix} E_y^I(x) \\ H_z^I(x) \end{bmatrix} = \mathbf{M}\left(x; k_t^0; Z_0\right) \begin{bmatrix} E_0 \\ 0 \end{bmatrix} \tag{12a}$$

$$\begin{bmatrix} E_y^{II}\left(\frac{d}{2} + x\right) \\ H_z^{II}\left(\frac{d}{2} + x\right) \end{bmatrix} = \mathbf{M}\left(x; k_t^1; Z_1\right) \begin{bmatrix} E_y^I\left(\frac{d}{2}\right) \\ H_z^I\left(\frac{d}{2}\right) \end{bmatrix} \tag{12b}$$

$$\begin{bmatrix} E_y^{III}\left(\frac{d}{2} + t + x\right) \\ H_z^{III}\left(\frac{d}{2} + t + x\right) \end{bmatrix} = \mathbf{M}\left(x; k_t^0; Z_0\right) \begin{bmatrix} E_y^{II}\left(\frac{d}{2} + t\right) \\ H_z^{II}\left(\frac{d}{2} + t\right) \end{bmatrix} \tag{12c}$$

where

$$\mathbf{M}\left(x; k_t^i; Z_i\right) = \begin{bmatrix} \cos\left(k_t^i x\right) & -j Z_i \sin\left(k_t^i x\right) \\ -j \frac{\sin(k_t^i x)}{Z_i} & \cos\left(k_t^i x\right) \end{bmatrix} \tag{13}$$

is the transmission matrix,

$$Z_i = \frac{\omega \mu_0}{k_t^i} \tag{14}$$

are the wave impedances, and

$$k_t^0 = \frac{2\pi}{\lambda_0} \sin\theta_0 = k_0 \sin\theta_0 \tag{15}$$

$$k_t^1 = \sqrt{k_1^2 - k_z^2} = k_0 \sqrt{n_1^2 - \cos^2\theta_0} \tag{16}$$

are the transverse propagation constants for a given excitation k_0 and angle of incidence θ_0.
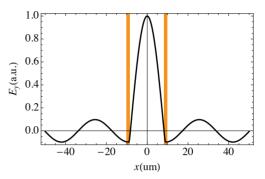

Figure 4: Electric field distribution in x.

Design

The input parameters are the laser wavelength $\lambda_0 = 10.6\,\mu\text{m}$, and the desired undulator wavelength $\lambda_u = 200\,\mu\text{m}$. Using those parameters, Equation (11) is solved for the waveguide wavelength $\lambda_G = 11.19\,\mu\text{m}$. All propagation constants can now be fully determined, and the incidence angle is:

$$\theta_0 = \arccos\left(\frac{k_z}{k_0}\right) = 18.73° \tag{17}$$

A choice for the distance d between the two thin p-Si films can be calculated such that the interface behaves as a perfect conducting surface:

$$d = \frac{\pi}{k_t^0} = 16.5\,\mu\text{m} \tag{18}$$

A choice for the p-Si film thickness, is such that the reflected power from the thin film is maximised. The ray that is reflected from the boundary between region I and region II changes polarity because the light travels from a medium with low refractive index, to a medium with high refractive index. To maximise reflected power, the reflected wave from the boundary between region II and region III has to interfere constructively with the reflection from the boundary between region I and region II. The condition for this is $2t k_t^1 = \pi$, which yields:

$$t = \frac{\pi}{2 k_t^1} = 806\,\text{nm} \tag{19}$$

Now, the design is fully specified, the transverse field profile can be calculated using Equations (12), which is shown in Figure 4. The peak electric field is limited by the dielectric strength of polysilicon which is 400 MV/m, [12]. The maximum peak field in the center is 4.09 GV/m, which from Equation (11) yields $K = 0.013$. Using a material with a higher dielectric strength as the optical layer, will help increase K.

(a) Step #1: Thin film deposition

(b) Step #2: Etch alignment marks

(c) Step #3: Pattern epi p-Si

(d) Step #4: Backside etch and vapor HF release

(e) Thin film SEM picture after step #4

(f) Step #5: Final bonding

(g) Mask #1 used for step #2

(h) Mask #2 used for step #3

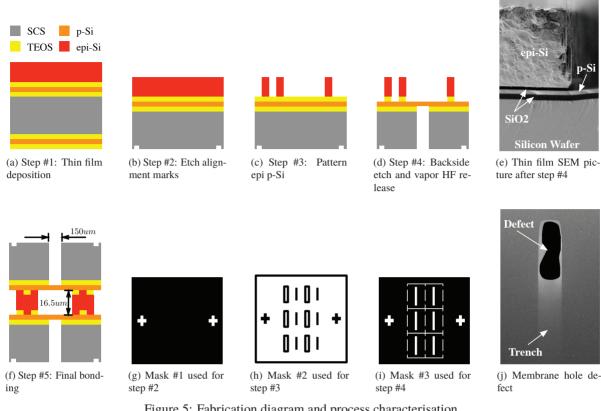(i) Mask #3 used for step #4

(j) Membrane hole defect

Figure 5: Fabrication diagram and process characterisation.

DEVICE FABRICATION

Fabrication Process

The device is fabricated on <100> SCS wafers (WRS Materials, R-Prime Wafers). After a standard pre-diffusion clean, wafers are coated with 1 μm of sacrificial SiO2 in a tetraethyl orthosilicate (TEOS) furnace (Tylan), running the standard TEOS process. The wafers are then coated with 806nm of p-Si, in an low pressure chemical vapor deposition (LPCVD) furnace (Thermco Systems), followed by coating with another 0.5 μm of sacrificial TEOS oxide. On the front side of the wafers, a 16 μm–thick epi p-Si layer, is grown at 1080℃ using dichlorosilane (DCS) in a epitaxial reactor (Applied Materials Centura). The epi p-Si growth is done in 5 steps, because the maximum allowed growth thickness between two chamber cleans is 3 μm. This stage of the wafer processing is depicted in Figure 5a.

Subsequently, the two TEOS oxide layers and the p-Si layer are removed from the backside of the wafers using dry etching (Applied Materials Precision 5000). The wafers go through a standard piranha clean, followed by a 30 seconds HF dip to clean the surface for lithography. Subsequently, the surface is vapor-primed with hexamethyldisilazane (HMDS) in a 150℃ oven (Yield Engineering Systems), and the back side is coated with 1 μm positive tone photoresist (Shipley 3612). The back side is exposed in a contact aligner (Electronic Visions 620), using the first mask to pattern alignment marks. A simplified model of the mask is depicted in Fig-

ure 5g. The photoresist is developed using the standard recipe for this photoresist, and the exposed area is etched 500nm deep, using dry etching (Applied Materials Precision 5000), to form the alignment marks for subsequent lithography steps. The photoresist is removed in microwave oxygen plasma (Gasonics Aura Asher). This stage of the wafer processing is depicted in Figure 5b.

The wafers go again through the standard piranha clean, 30 seconds HF dip, and HMDS oven, to prepare for lithography. The front side is coated with 1.6 μm positive tone photoresist (Shipley 3612) and the wafers are exposed, aligning the second mask to the alignment marks on the backside. The second mask is used to pattern the epi p-Si, and a model of the mask is shown in Figure 5h. The photoresist is developed using the standard recipe for this photoresist, and the exposed area is etched all the way until the sacrificial TEOS oxide, in a deep reactive ion etching (DRIE) tool (Surface Technology Systems Inductively Coupled Plasma), and the photoresist is removed in microwave oxygen plasma. This stage of the wafer processing is depicted in Figure 5c. Figure 5e shows a cross section of the films at this stage of processing from a wafer that was cleaved.

The wafers go again through the standard Piranha clean, 30 seconds HF dip, and HMDS oven, to prepare for lithography. The back side is coated with 7 μm positive tone photoresist (SPR 220-7) and processing is stopped for at least 24 hours, for the resist to outgas. The wafers are then exposed, aligning the third mask to the alignment marks on

(a) Sample #1 measurement vs model
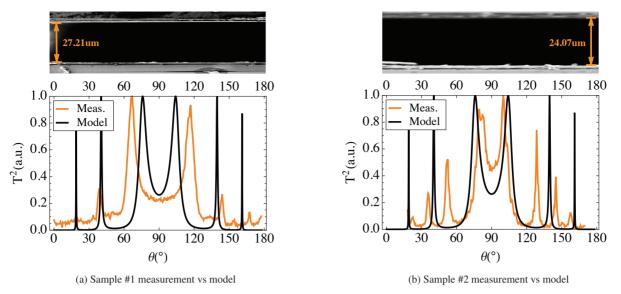

(b) Sample #2 measurement vs model

Figure 6: Sample measurements (inset shows the SEM measured gap between the dielectric plates).

the backside. The third mask is used to define the trench opening, and a model of the mask is shown in Figure 5i. The photoresist is developed using the standard recipe for this photoresist, and the exposed area is etched all the way until the sacrificial TEOS oxide, in a DRIE tool. At this point the wafer is almost etched thought, and has many pieces connected together with small silicon bridges. These bridges are cracked manually to dice the wafer. The photoresist is removed from the backside of the pieces in microwave oxygen plasma, using a carrier wafer that has a pocket etched. Subsequently, the sacrificial TEOS oxide is removed from all open areas using anhydrous vapor HF and ethanol (SPTS uEtch). This stage of processing is depicted in Figure 5d. Finally, the pieces are taken out of the cleanroom and assembled together. Epoxy is applied on the sides of the stack to keep the pieces together. The final devices are depicted in Figure 5f

Choice of Materials & Processes Discussion

The fabrication process was significantly affected by the availability of materials and tools at SNF. For the substrate, silicon was chosen in order to simplify the fabrication, since SNF is mainly a silicon laboratory. Other options such as germanium or cadmium telluride, that are transparent in the wavelength of interest, were more expensive, and would create complications for processing in SNF. However because silicon is not entirely transparent, it follows that a backside trench must be formed in order to deliver most of the light to the waveguide. For the optical layer, polycrystalline silicon was chosen since it is transparent and has low absorbance in the wavelength of interest, unlike silicon oxide and silicon nitride. Other materials that are suitable for this application, like titanium dioxide, could only be deposited with atomic layer deposition (ALD) tools, thus limiting the thickness to less than 50nm, which is far from what is required for

this device. The epi p-Si layer was used, since it was the only process available that could deposit a 16 µm–thick layer to be used a spacer. This layer was etched in a DRIE tool, because it was the only available tool, that could etch 16 µm of silicon, without burning the photoresist.

The greatest issue that was encountered during fabrication, was the stress between the two sacrificial layers and p-Si layer that caused it to crack. Initially thermal oxide was used as the first sacrificial layer. After the DRIE step to open the backside trench, most of the epi p-Si membranes on the top of the trench where either completely gone, or cracked. The membranes that were left, where destroyed in the subsequent dicing of the wafer – due to vibrations – and removal of the sacrificial layers. Low stress silicon nitride was also investigated as an alternative, since it is very strong material and indeed all membranes were intact after the DRIE step. However, removing the silicon nitride – which is vey absorbing material – with dry etching caused the membranes to crack. TEOS oxide has very low stress since it is deposited at low temperature and more than 70% of the membranes survived the DRIE and wafer dicing steps. Finally removing the sacrificial layers with vapor HF, instead of wet or dry etching with plasma, allowed around 50% total yield. In some of the successfully fabricated devices, there are still some minor cracks at the edges of the trench, however, that position is shaded by the height of the trench, and therefore does not affect operation. Such a defect is shown in Figure 5j.

Another issue, was that the pieces did not correctly align during the last assembly step, resulting in larger gaps, and not perfectly parallel plates. The reasons for that were big silicon particles from the dicing of the wafer, and tolerances in the patterning of the epi p-Si layer, in which a transparency mask was used.

COLD TESTS

To validate the presented model of the undulator, optical power transmission measurements were performed at different angles of incidence. The device was mounted on a rotating stage, as shown in Figure 7. The output of an optical parametric amplifier (OPA), tuned at $10.6 \mu m$ to emulate a carbon dioxide (CO2) laser, was focused on the sample slit, and the transmitted power was measured at the detector. The entire transmission model for different angle of incidence θ_0 can be obtained using Equations (12), (13), (14), (15), and (16):

$$\begin{bmatrix} (1+R) E_i \\ (1-R) \frac{E_i}{Z_0} \end{bmatrix} = \mathbf{M}_t \begin{bmatrix} T E_i \\ T \frac{E_i}{Z_0} \end{bmatrix} \quad (20a)$$

$$\mathbf{M}_t = \mathbf{M}\left(t; k_t^1; Z_1\right) \mathbf{M}\left(d; k_t^0; Z_0\right) \mathbf{M}\left(t; k_t^1; Z_1\right) \quad (20b)$$

where R and T are the field reflection and transmission coefficients. Equations (20) are solved for T, and the total power transmission coefficient is T^2.
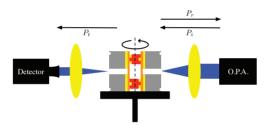

Figure 7: Transmission Measurement Setup.

Two undulators were assembled, and optical transmission measurements were performed using the setup in Figure 7. The measurements from the two samples are shown in Figure 6. The measurements were normalised to the maximum power measurement, since a fraction of power was not transmitted due to poor focusing and shading at the backside trench. The samples were also analysed under SEM, in order to measure the gap and film thickness. The measured thickness was 872 nm, which is in good agreement with the design value in Equation (19), given that the fabrication occurred in an experimental facility. The measured gaps however, deviated significantly because of alignment issues. Overall, the measurements are in agreement with the model in terms of the number of peaks and their relative positions, however there are differences because of the dielectric plates not being parallel.

CONCLUSION

In this work, a novel laser-driven undulator with $200 \mu m$ undulator wavelength was proposed, and the analytical model for the undulator was derived. The fabrication process was presented, and optical transmission measurements in fabricated devices were performed to validate the model. Certain parts of the fabrication process need to be re–worked, before proceeding to hot tests.

REFERENCES

[1] Z. Huang and K.-J. Kim, "Review of x-ray free-electron laser theory," *Phys. Rev. ST Accel. Beams*, vol. 10, p. 034801, Mar 2007.

[2] Y. Ivanyushenkov *et al.*, "Development of a superconducting undulator for the aps," *Journal of Physics: Conference Series*, vol. 425, no. 3, p. 032007, 2013.

[3] S. Bellucci *et al.*, "Experimental study for the feasibility of a crystalline undulator," *Phys. Rev. Lett.*, vol. 90, p. 034801, Jan 2003.

[4] S. Tantawi *et al.*, "Experimental demonstration of a tunable microwave undulator," *Phys. Rev. Lett.*, vol. 112, p. 164802, Apr 2014.

[5] R. J. Loewen, "A compact light source: Design and technical feasibility study of a laser-electron storage ring x-ray source," Ph.D. dissertation, Stanford University, 2003.

[6] A. Debus *et al.*, "Traveling-wave thomson scattering and optical undulators for high-yield euv and x-ray sources," *Applied Physics B*, vol. 100, no. 1, pp. 61–76, 2010.

[7] V. Karagodsky and L. Schächter, "High efficiency x-ray source based on inverse compton scattering in an optical bragg structure," *Plasma Physics and Controlled Fusion*, vol. 53, no. 1, p. 014007, 2011.

[8] T. Plettner and R. L. Byer, "Proposed dielectric-based microstructure laser-driven undulator," *Phys. Rev. ST Accel. Beams*, vol. 11, p. 030704, Mar 2008.

[9] Stanford nanofabrication facility website. [Online]. Available: http://snf.stanford.edu

[10] S. F. Mahmoud, *Electromagnetic Waveguides: theory and applications*. IET, 1991.

[11] T. Shintake, "Experimental results of microwave undulator," *Proc. SPIE*, vol. 0582, pp. 336–343, 1986.

[12] R. J. England *et al.*, "Manufacture and testing of optical-scale accelerator structures from silicon and silica," *Proc. 3rd Int. Particle Accelerator Conf.*, 2012.